Theoretical tensile strength of an Al grain boundary

Guang-Hong Lu,* Shenghua Deng, and Tianmin Wang
School of Science, Beijing University of Aeronautics and Astronautics, 37 Xueyuan Road, Haidian District, Beijing 100083, People's Republic of China

Masanori Kohyama
Special Division for Green Life Technology, National Institute of Advanced Industrial Science and Technology, 1-8-31 Midorigaoka, Ikedashi, Osaka 563-8577, Japan

Ryoichi Yamamoto
Institute of Industrial Science, University of Tokyo, 4-6-1 Komaba, Meguro-ku, Tokyo 153-8505, Japan
(Received 29 December 2003; published 15 April 2004)

The *ab initio* tensile test has been applied to an Al $\Sigma 9$ grain boundary by using the *ab initio* pseudopotential method. The theoretical tensile strength is 9.50 GPa at the strain 21%. As compared with the theoretical tensile strength in the direction [001] or [111] of an Al single crystal, the boundary is still strong due to the interface reconstruction. The interface extends at almost the same rate with the bulk interlayer until the strain of 19% in spite of the reduced number of interfacial bonds, which indicates the special strength of the reconstructed bonds. This feature can be regarded as a typical property of Al that strong local bonds are formed for less-coordinated atoms at defects.

DOI: 10.1103/PhysRevB.69.134106 PACS number(s): 62.20.Mk, 61.72.Mm, 61.72.Bb, 73.20.−r

I. INTRODUCTION

The theoretical (ideal) strength of a crystal is determined by the maximum stress at elastic instability (yield or break) when applying an increasing stress to an infinite, perfect (defect-free) crystal.[1] It forms an upper limit to the strength of a real crystal, which is of both scientific and engineering value. The theoretical strength is an intrinsic material property, which is determined by the behavior of valence electrons and ions. Similarly, the theoretical strength of an ideal defective system containing only one defect such as a point defect, an interface, a grain boundary, etc., can be determined as the maximum stress required to reach elastic instability under increasing load without introducing extrinsic dislocations or cracks. This can be regarded as intrinsic local strength of a defect region in real materials. It is of great importance to investigate such theoretical strength of both perfect and defective systems in order to understand the mechanical properties of materials.

By virtue of the development of the density-functional theory (DFT)[2,3] combined with the band-theoretical schemes and the rapid progress of modern computers, *ab initio* methods can be applied to calculate the theoretical strength and mechanical behavior of materials. About bulk crystals, all-electron methods such as the full-potential (FP) linear muffin-tin orbital (LMTO) method with the atomic-sphere approximation (ASA) or full-potential linearized augmented plane wave (FLAPW) method have been used for metallic crystals such as W, Cu, Ir, and NiAl.[4–6] Recently the *ab initio* pseudopotential method has been applied to the theoretical tensile or shear strength of a lot of crystals such as Al,[7–9] SiC,[10] Si_3N_4,[11] Cu,[7] W,[12] diamond, Si and Ge,[13] Mo and Nb,[14] and also MoSe nanowires.[15] Some results can be compared directly with that by the nanoindentation experiment.[16]

The *ab initio* pseudopotential method can now deal with larger systems by coupling with recent new algorithms.[17–19] This kind of scheme can be applied to the theoretical strength and mechanical behavior of defective systems in addition to perfect crystals, although there exist only a few applications to defective systems even at present. To our knowledge, theoretical tensile strength of Al with an atomic-scale void[9] and that of a tilt grain boundary of cubic SiC with nonpolar and polar interfaces[20,21] have been examined through *ab initio* tensile tests. And also theoretical shear strength and sliding behavior of a twist grain boundary in Ge (Ref. 22) and of tilt and twist boundaries in Al (Ref. 23) have been examined through *ab initio* shear tests. (Here we call an *ab initio* calculation of theoretical tensile strength as *ab initio* tensile test, and of theoretical shear strength as *ab initio* shear test.)

In our previous work,[24–29] the effects of impurities Na, Ca, Si, and S on an Al grain boundary have been investigated by the *ab initio* pseudopotential method based on the local density functional theory. These impurities have been experimentally found to have embrittlement effects on an Al boundary. The embrittlement mechanisms of respective impurity have been classified into different models, i.e., decohesion model or bond mobility model through their different electronic and structural effects in the ground state. However, as pointed out in our previous work, it is of great importance to perform *ab initio* tensile test and *ab initio* shear test of grain boundaries with these impurities so as to determine the embrittlement mechanisms by these impurities more accurately. In this paper, an *ab initio* tensile test has been performed on a clean Al grain boundary as a first step.

Usually Al is regarded as a typical simple metal. However, recent *ab initio* calculations have clarified the peculiar nature of Al different from other simple metals. For example, the calculated binding energy of a divacancy in Al is nega-

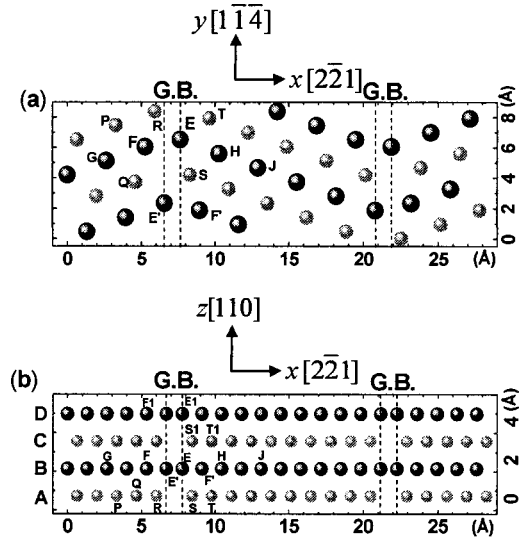

FIG. 1. Top view (a) and side view (b) of the supercell of Al Σ 9 $(2\bar{2}1)/[110]$ tilt grain boundary. The lengths of three sides are 28.469, 8.379, and 5.586 Å, respectively. The supercell contains 84 atoms, which are in four (110) atomic layers, i.e., A, B, C, and D, whose face distance is the same as that of (110) in fcc-Al (about 1.397 Å). Layers C and D are equivalent to layers A and B, respectively, due to the double period in the [110] direction. The dark-gray spheres indicate the atoms in the B (D) layer. The light-gray spheres indicate the atoms of the A (C) layer. Some atoms are marked for later discussions.

tive, because of the stabilization of a monovacancy due to the formation of strong Al-Al bonds with some covalent characters at the first shell,[30] which is quite different from other simple metals such as Mg.[31] The formation of strong local bonds with some covalent characters for less-coordinated or distorted atoms in Al has been also observed in Al surfaces[32] and shear distortion of Al.[33] We will show in this paper that interfacial bonds in the present Al grain boundary have also such kind of characteristics.

In this paper, the supercell construction and computational method are explained in Sec. II, followed by Sec. III: results and discussion. The conclusions are made in the last section.

II. SUPERCELL CONSTRUCTION AND COMPUTATIONAL METHOD

The supercell is the same as our previous reports,[24–29] as shown in Fig. 1, where x, y, and z axes are $[2\bar{2}1]$, $[1\bar{1}\bar{4}]$, and [110] directions, respectively. An Al $\Sigma 9$ $(2\bar{2}1)/[110]$ tilt grain boundary is formed by rotating one grain by 38.94° along the [110] axis, and $(2\bar{2}1)$ is set as the boundary plane. The coincidence site lattice (CSL) supercell on the boundary plane is defined by $(3\sqrt{2}/2)\,a_0$ in the $[1\bar{1}\bar{4}]$ direction and $(\sqrt{2}/2)\,a_0$ in the [110] direction, respectively, where a_0 is the lattice constant of Al obtained by the present scheme. The size in the [110] direction is set twice as large as that of the CSL, i.e., $\sqrt{2}a_0$. This double size is adopted so as to introduce impurity atoms at the interface without neighboring to each other. In the present study, we use the same cell in order to make a comparison with future tensile tests with impurities. In the $[2\bar{2}1]$ direction, two symmetric boundaries are introduced to make the periodicity. There are four (110) atomic layers in the supercell, A, B, C, and D. Layer A is equivalent to layer C and layer B is equivalent to layer D because of the double period.

The rigid-body translation parallel to the interface can make both the glide-plane and mirror-pane symmetry models. In the high-resolution electron microscopy (HRTEM) observation,[34] both types of configurations seem to exist in Al. The energy calculation using the EAM potential has indicated the relative stability of the glide-plane symmetry model.[34] A configuration with similar glide-plane symmetry is also stable for the same $\Sigma 9$ boundary in SiC, to which the *ab initio* tensile test has been applied.[20–21] Therefore we deal with the configuration with the glide-plane symmetry in this study. The present initial atomic configuration is similar to the observed one by the HRTEM.[29]

We employ the standard pseudopotential total-energy method[35] based on the DFT (Refs. 2 and 3) the local-density approximation (LDA).[36,37] The wave functions are obtained by solving the Kohn-Sham equation using a plane wave basis. The plane-wave kinetic energy cutoff is 15 Ry. The electronic ground state is obtained efficiently using the conjugate-gradient technique proposed by Bylander, Kleinman, and Lee[38] with the Kerker mixing scheme.[39] This method has been shown very efficient for determining the minimum of the Kohn-Sham total-energy functional for large systems containing metallic bonding.[40] For summation over Brillouin zone, a uniform grid of 32 **k** points is chosen according to the Monkhorst-Pack scheme.[41] The electronic density is determined in a real space grid of $256\times64\times32$ points.

The *ab initio* semirelativistic ionic pseudopotential of Al with norm conserving conditions is constructed through the Troullier-Martins scheme[42] with the atomic electronic configuration $3s^{1.0}3p^{0.5}3d^{0.5}$ and cutoff radii 1.80, 2.00, and 2.00 (a.u.) for the s, p, and d components, respectively.[43] The separable form by Kleinman and Bylander[44] is used with the p orbital as the local component. The lattice constant calculated by the generated pseudopotential is 3.95 Å for fcc Al, which is in good agreement with the corresponding corrected experimental value of 4.02 Å at absolute 0 K.[45]

In the *ab initio* tensile test, the Hellman-Feynman theorem is adopted to determine the tensile stress through the Nielsen-Martin scheme.[46] The quasistatic energy E_{total} ($T=0$ K) of the deformed grain boundary and the Hellman-Feynman stresses $\sigma_{\alpha\beta}$ $(\alpha,\beta=1,2,3)$ on the supercell are calculated using the pseudopotential total-energy scheme within the LDA. According to the Nielsen-Martin scheme, the stress $\sigma_{\alpha\beta}$ is calculated from

$$\sigma_{\alpha\beta}=\frac{1}{\Omega}\frac{\partial E_{\text{total}}}{\partial \varepsilon_{\alpha\beta}}, \tag{1}$$

where $\varepsilon_{\alpha\beta}$ is the strain tensor $(\alpha,\beta=1,2,3)$, and Ω is the volume of the supercell.

In the tensile test, a uniaxial tensile strain is introduced into the stable configuration. The supercell is stretched by a

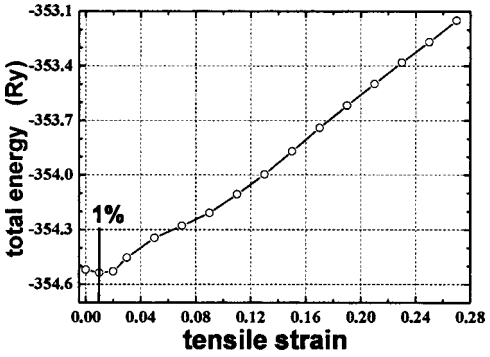

FIG. 2. Total energy as a function of tensile strain in the *ab initio* tensile test of the Al Σ9 grain boundary.

small increment in the $[2\bar{2}1]$ direction that is normal to the boundary plane. The strain is determined by

$$\varepsilon = (l_\varepsilon - l_0)/l_0, \tag{2}$$

where l_ε is the length of the cell in the $[2\bar{2}1]$ direction with the strain ε and l_0 is that of the initial cell. The cell lengths in the $[1\bar{1}4]$ and [110] directions are fixed in order to reduce the computational time, which implies that Poisson's ratio is not considered in the tensile test. In other words, the present load is not uniaxial *tension* but uniaxial *extension*. The basis vectors $\vec{a}_1$, $\vec{a}_2$, and $\vec{a}_3$ in the $[2\bar{2}1]$, $[1\bar{1}4]$, and [110] directions, respectively, defining the supercell then become

$$\vec{a}_1 = (1+\varepsilon)a_0\hat{x}, \quad \vec{a}_2 = \frac{3\sqrt{2}}{2}a_0\hat{y}, \quad \vec{a}_3 = \sqrt{2}a_0\hat{z}, \tag{3}$$

where $\hat{x}$, $\hat{y}$, and $\hat{z}$ are unit vectors in the $[2\bar{2}1]$, $[1\bar{1}4]$, and [110] directions, respectively. In each strain step, starting atomic positions for relaxation are taken by uniform scaling from the relaxed coordinates of the preceding step, which is necessary to ensure the continuous strain path. All the atoms are relaxed according to the Hellman-Feynman forces until all the forces are less than 0.05 eV/Å. After that, the total energy and stress tensor are calculated. This cycle is iterated until the stress reaches the maximum value and the failure starts. During the tensile test, the symmetric property of the system is naturally preserved. For example, all the atoms are located on four (110) layers in the cell and there occurs no displacement deviating from such layers.

This procedure corresponds to a real tensile test at zero temperature. Therefore phonon-induced dynamic instability is not considered in the present calculation. The tensile strength computed here refers to the limit of internal stability under quasistatic deformation in the low-temperature limit.

III. RESULTS AND DISCUSSION

A. Theoretical tensile strength

The total energy as a function of tensile strain is shown in Fig. 2. Total energy decreases at the strain 1%, and then increases. This is due to the boundary expansion after the initial relaxation, as shown in Fig. 3. The initial interface distance is set as the bulk interlayer distance, which determines the initial cell size along the $[2\bar{2}1]$ direction. In the initial relaxation, almost all the atoms at the right of the boundary move to the right ($[2\bar{2}1]$ direction), and almost all the atoms at the left of the boundary move to the left ($[\bar{2}\bar{2}1]$ direction). The moving distance of the atoms near the boundary is larger than that of the atoms far from the boundary. For example, atom E moves to the right by about 0.10 Å, 0.35% of the cell size in this direction, while atom F moves to the left by about 0.12 Å, 0.42% of the cell size in this direction. Therefore, there exists the residual *compressive* stress in the supercell, as will be shown. When the supercell is stretched, the residual stress is relaxed at first, and thus the total energy becomes a little lower.

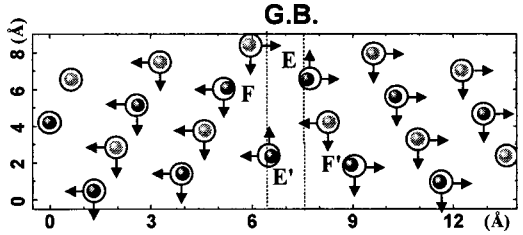

FIG. 3. The relaxed configuration of the left half part of layer B(D) and A(C) in the supercell without strain. E, F and E′, F′ correspond to the atoms marked in Fig. 1. Atom positions of the initial supercell are represented by the smaller spheres, in which the dark-gray and light-gray ones represent the atom positions of B(D) and A(C) layer, respectively. The bigger circles indicate atom positions after the relaxation. The arrows indicate the direction of atoms moving after the relaxation.

The tensile stress of the Al grain boundary as a function of tensile strain is shown in Fig. 4. The stresses in the $[2\bar{2}1]$, $[1\bar{1}4]$, and [110] directions are plotted. All the shear components of the stress tensor are negligible (lower than 10^{-6} GPa) and can be regarded as zero at the error range. This is due to the symmetry of the present cell with the uniaxial tensile strain.

The tensile stress along the $[2\bar{2}1]$ direction, normal to the interface, reveals the theoretical tensile strength of the present boundary. However, tensile stresses along the $[1\bar{1}4]$ and [110] directions parallel to the boundary plane are also generated, as shown in Fig. 4. This is because the present load is not uniaxial *tension* but uniaxial *extension*, as mentioned above. This condition is similar to the previous *ab initio* tensile tests on a SiC grain boundary[20,21] and an Al single crystal with an atomic void.[9] In order to realize uniaxial *tension*, the cell sizes along these two directions should be adjusted (reduced) in each step, naturally according to the Poisson's ratio, so that the stresses in these two directions become zero. The present *extension* process is equivalent to loading tension along these two directions to prevent such contraction. This should overestimate the theoretical tensile strength as the case of a tensile test of bulk crystal.[47]

There remain small compressive stresses in the initial supercell with the strain 0%, as shown in Fig. 4. In the $[2\bar{2}1]$ direction, the compressive stress is as high as 3.99 GPa, nearly twice as large as that in the $[1\bar{1}4]$ direction, 1.96 GPa,

TABLE I. The theoretical tensile strength σ_{max} and the corresponding strain ε_{max}.

Al	ε_{max}	σ_{max} (GPa)
[001][a]	20%	11 ± 1
[001][b]	36%	12.54
[111][b]	29.5%	11.05
$\Sigma 9$ Grain Boundary[c]	$21\% \pm 1$	9.50
Filament[d]	2.9%	2.25

[a]Reference 8.
[b]Reference 10.
[c]Present calculation.
[d]Reference 48.

and about four times larger than that in the [110] direction, 1.04 GPa. The compressive stress in the $[2\bar{2}1]$ direction is caused by the boundary expansion in the relaxation of the initial supercell as mentioned above. The lower compressive stresses in the $[1\bar{1}4]$ and [110] directions at the strain 0% should be generated as a result of the compression along the $[2\bar{2}1]$ direction. The difference in the magnitudes of the two components may be caused by some geographic anisotropy of the present configuration as observed in the tensile test of a $\Sigma 9$ $(2\bar{2}1)/[110]$ tilt boundary in SiC.[20,21]

It is shown in Fig. 4 that the tensile stress normal to the interface increases with the increase of the tensile strain. At the strain 21%, the stress reaches the maximum value, about 9.50 GPa. After this strain, the stress decreases. Therefore the theoretical tensile strength of the Al $\Sigma 9$ grain boundary is 9.50 GPa, which is the upper bound of the tensile strength of this boundary.

Table I lists the theoretical tensile strength σ_{max} and the corresponding maximum strain ε_{max} of an Al single crystal. All were obtained by the *ab initio* pseudopotential method. There are, unfortunately, no tensile strength results of Al single crystal in the $[2\bar{2}1]$ direction, which should be directly compared with our results. However, the theoretical tensile strength in the [001] and [111] directions listed in Table I indicates that the magnitude of the strength of the Al single crystal may not be so dependent on the tensile directions. Because a grain boundary contains a disordered interfacial configuration, the theoretical tensile strength should be lower than that of the perfect crystal. The maximum tensile stress of the present Al boundary, i.e., 9.50 GPa by our calculation is a bit lower than that in the [100] or [111] direction of the perfect Al crystal. This means that the present boundary is rather strong. This is due to the reconstructed interfacial bonds, which will be discussed in detail in the following subsections. Here it should be noted that the present relation between the tensile strength of the boundary and that of the perfect crystal is similar to the previous results of the reconstructed interfaces of the $\Sigma 9$ $(2\bar{2}1)/[110]$ tilt grain boundary in SiC,[20,21] where the values of the tensile strength are 48 and 42 GPa for polar and nonpolar interfaces, respectively, as compared with that of the perfect SiC crystal, 50.8 GPa, in the [111] direction.

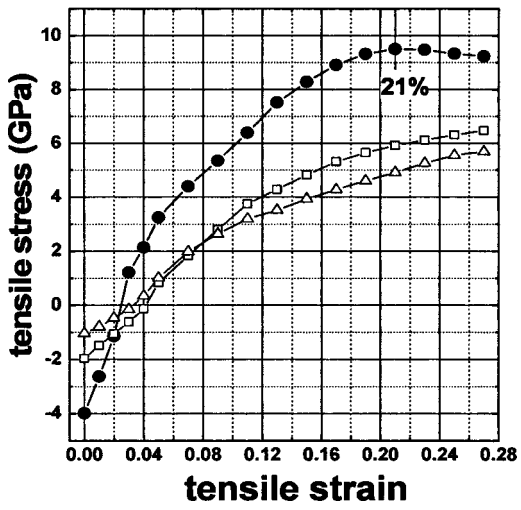

FIG. 4. Tensile stress as a function of tensile strain of the Al Σ 9 grain boundary. The filled circles, squares, and triangles indicate the stress in $x[2\bar{2}1]$, $y[1\bar{1}4]$, $z[110]$ directions, respectively.

On the other hand, it is not so easy to judge the accuracy of our results by direct comparison with experiments. There are no comparable experimental data of Al samples containing only grain boundaries (dislocation free). The range of the tensile strength of polycrystalline Al sheets in the different conditions is from 55 to 145 MPa at the elongation from 10 to 55%,[49] much lower than that of the present boundary. However, the tensile strength of an Al filament tested by Gane[48] is much higher. The width of the Al filament (single crystal) used by Gane is 10.0 μm and the thickness is 0.66 μm. The maximum tensile stress is 2.25 GPa at the maximum elastic strain 2.9%. But this is still much smaller than the strength of the bulk crystal listed in Table I and the present boundary. This is because the dislocation motion dominates the strength of these experimental samples. In real crystals, the major defects inside the grain are dislocations, the motion of which usually results in a considerable reduction in strength as compared with ideal strength without any dislocations.[50]

After the maximum tensile stress at the strain of 21%, the stress decreases very slowly. This is different from the polar interface of the $\Sigma 9$ boundary in SiC with similar glide-plane symmetry,[21] where the stress decreases rapidly after the maximum stress (48 GPa) at the strain 14%. This suggests the different characteristics between metallic bonds and covalent bonds. SiC is a typical covalent-bonding material. In covalent materials, atoms are bound by shared valence electrons, and the bond has strong directional properties. The covalent bond is generally stronger than the metallic bond, and in the case of bond breaking, the strength decreases rapidly. However, Al is a typical sp-valent metal, where valence electrons are less localized as compared with covalent materials. Although the interfacial bonds of the present interface have different features as will be discussed, the stress-strain curve in Fig. 4 seems to reveal basically metallic features. Similarly, in Fig. 2, the energy is still increasing after the maximum tensile strength at 21%, which means the system is still unstable. This infers that the failure has not been completed.

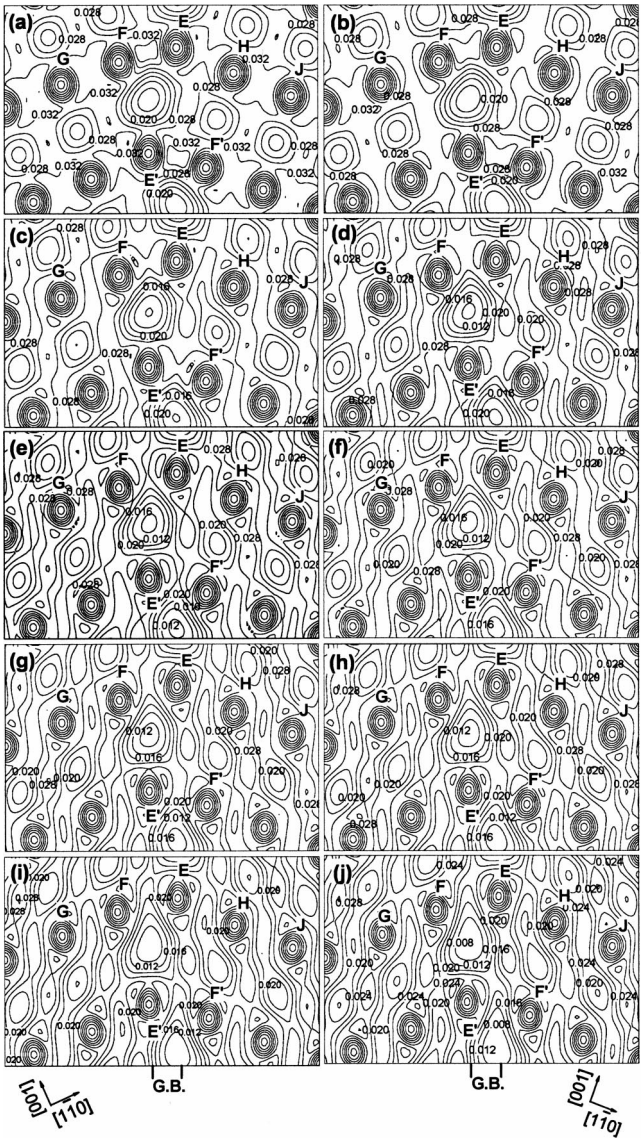

FIG. 5. The valence charge density distribution of the left half part of the B layer in the supercell at the strain (a) 0%, (b) 3%, (c) 9%, (d) 13%, (e) 15%, (f) 17%, (g) 19%, (h) 21%, (i) 25%, (j) 27%, respectively. The interval of the contours is $0.004e$/a.u.^{3}

B. Valence charge density

In metallic systems, valence charge density distribution reveals the features of local atomic bonds. We analyze the charge density of layer B containing boundary atoms as shown in Fig. 1. Figure 5 shows the charge density distributions in the left half part of layer B on the [110] cross section with the increase of the strain. Figure 6 shows the charge density of perfect fcc-Al on the [110] cross section. It should be noted that the $[1\bar{1}0]$ direction is one of the most closely packed directions. In the present boundary, EH, HJ, and FG bonds, for example, correspond to this kind of first-neighbor $[1\bar{1}0]$ bond. If comparing the charge density of the boundary at the strain 0% [Fig. 5(a)] with that of perfect Al, the charge density at such $[1\bar{1}0]$ bonds of the boundary is higher. This is because the bulk regions in the supercell are slightly compressed by the boundary expansion after the initial relaxation as mentioned above. Thus at the strain 3% [Fig. 5(b)] where the compression is relaxed, the charge density at the $[1\bar{1}0]$ bonds is in a similar range to that of perfect Al.

In Fig. 5, EF and symmetrically equivalent E′F′ bonds are the interfacial reconstructed bonds. At the strain 0%, the charge density at the EF bond is greater than $0.036e$/a.u.^{3} This is the highest one as compared with the charge density values at the $[1\bar{1}0]$ bonds such as FG, EH, and HJ, which are all intervening between $0.032e$/a.u.^{3} and $0.036e$/a.u.^{3} At the strain 3%, the EF bond still has the highest density value. The increased bond charge at the EF bond center has features rather similar to covalent materials such as Si. However, there exists a low-density region between the EF and E′F′ bonds at the interface. In this region, the charge density is as lower as $0.012e$/a.u.^{3} at the strain 0%.

An atom in fcc structure has 12 nearest neighbors. At the interface, atom E loses 5 and atom F loses 3 of them before the interface formation. Namely, atom E has only 7 nearest neighbors left and atom F has only 9 left. Through the interface formation, atom E recovers three neighbors across the interface, namely, atom F and atoms R in the two different layers. Atom F recovers only one neighbor, namely, atom E. As compared with the interlayer between the bulk $[2\bar{2}1]$ layers, the number of first-neighbor bonds across the interface is clearly reduced and the directions of reconstructed bonds are different, which results in the formation of the low-density region at the interface. However, as shown in Fig. 5, the reconstructed EF and E′F′ bonds seem to be rather strong with increased bond charge. This should be involved in the large tensile strength of the present boundary comparable to that of ideal crystal.

With the strain increasing, the charge density decreases. The charge density at the EF bond remains the highest until the strain 13%, as shown in Figs. 5(b)–5(d). For example, at the strain 9%, the charge density at the EF bond is higher than $0.028e$/a.u.^{3}, but that of FG, EH, and HJ is lower than $0.028e$/a.u.^{3} At the strain 13%, the charge density at the EF bond is still higher than $0.024e$/a.u.^{3}

For the strains 15, 17, and 19 % [Figs. 6(e)–6(g)], the low-density region near the EF bond as mentioned above expands near the interval of the charge at the EF bond. Thus the charge density at the EF bond is in a similar range to that of the other $[1\bar{1}0]$ bonds (FG, EH, and HJ). The density values are all higher than $0.020e$/a.u.^{3} and lower than $0.024e$/a.u.^{3} at the strains 15 and 17 %.

These features of the charge density at the EF bond indicate that this reconstructed bond sustains the tensile stress at least until 19%. However, for the strain over 19%, as shown in Figs. 6(h)–6(j), the charge density at the EF bond decreases more rapidly than the other $[1\bar{1}0]$ bonds. It reaches as low as nearly $0.012e$/a.u.^{3} at the strain 25% and $0.008e$/a.u.^{3} at the strain of 27%. The low-density region extends further to the interval at the EF bond. It seems that the failure will be completed if the low-density region extends throughout the interface. On the other hand, the charge density at the FG, EH, and HJ bonds decreases gradually between $0.020e$/a.u.^{3} and $0.016e$/a.u.^{3} for the strain over

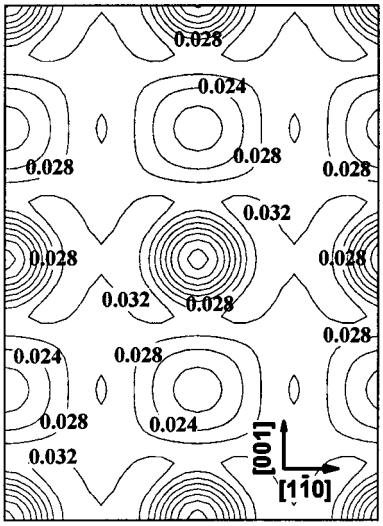

FIG. 6. The valence charge density distribution of fcc-Al on the (110) cross section. The interval of the contours is $0.004e/\text{a.u.}^3$.

19%. Note that the strain 21%, where the rapid decrease of the EF bond charge apparently starts, corresponds to the strain of the maximum tensile stress. This indicates that the breaking of the reconstructed EF bond mainly dominates the strength of the present boundary. In other words, the breaking of the EF bond mainly means the failure of this boundary.

C. Bond length

Figure 7 shows the changes of the bond lengths of the interfacial reconstructed EF bond and the back bonds of the EF bond as a function of the tensile strain. Only the symmetrically independent bonds are shown. EH, ET, and ES are the back first-neighbor bonds of atom E, and FG, FP, FQ, and FR are the back first-neighbor bonds of atom F. The vertical axes in Fig. 7 are set as

$$\frac{l-l_{\text{Al}}}{l_{\text{Al}}}\times 100, \tag{4}$$

where l is length of the bond during the tensile test and l_{Al} is the bond length of perfect fcc-Al, i.e., 2.793 Å from the present calculation.

First we consider the length change of the EF bond, namely, the interfacial reconstructed bond. At the strain 0%, the EF bond length is 2.659 Å, 4.8% shorter than that of perfect Al. At the strain 3% where the compressive stress is removed, this bond is still shorter than the bulk bond length. These facts as well as the charge density analyzed above suggest that the reconstructed EF bond be stronger than usual bonds. With the strain increasing, the EF bond extends almost linearly until the strain 19%. At the strain 19%, the EF bond length is 3.145 Å, 12.6% longer than that of perfect Al. At the strain 21% revealing the maximum stress, the EF bond is 3.229 Å, 15.6% longer than that of perfect Al. From 21%, the EF bond extends rapidly. It elongates to 3.606 Å, 29.1% longer than that of perfect Al at the strain 27%.

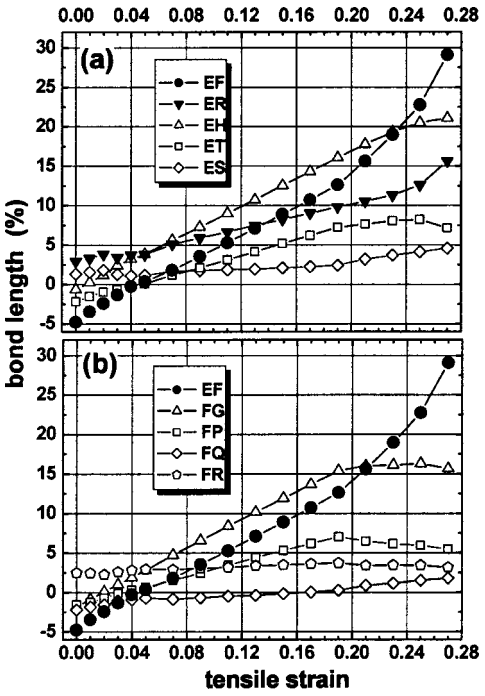

FIG. 7. The bonds length as a function of strain during the *ab initio* tensile test of Al $\Sigma 9$ grain boundary. The bonds length between atom E and its nearest neighbor are shown in (a), and that between atom F and its nearest neighbor are shown in (b). The length of the reconstructed EF bond is shown in both (a) and (b) for comparison.

About the back bonds of atom E [Fig. 7(a)], the EH and ET bonds are 0.6 and 2.2 % shorter than that of perfect Al, and the ES bond is 1.3% longer than that of perfect Al at the strain 0%. As shown in Fig. 7(a), the EH bond extends almost linearly until the strain over 21%. It is quite interesting that the linear coefficient of the EH bond extension is similar to that of the EF bond until 19%. For the strain over 21%, the increase of the EH bond length becomes slower, and the EH bond become shorter than the EF bond at the strain over 23%. On the other hand, the ET bond length increases very slowly with the strain increasing until the strain 25%, after which it contracts. The ES bond is almost unchanged until 19%.

About the back bonds of atom F [Fig. 7(b)], the lengths of FG, FP, and FQ at the strain 0% are 1.8, 1.6, and 2.2 % shorter than that of perfect Al, respectively, while the FR bond is 2.5% longer. As shown in Fig. 7(b), the FG bond extends almost linearly until the strain 19%. It is also quite interesting that the linear coefficient of the FG bond extension is similar to those of the EF and EH bonds until 19%. For the strain over 19%, the increase of the FG bond length almost stops, and this bond contracts at the strain 25%. On the other hand, the increases of the FP and FQ bond lengths are slow, and the FR bond is almost unchanged.

In Fig. 7, the length of the interfacial EF bond has a rapid increase (deviation from the linear increase) from the strain 21%. By considering the changes in the charge density distribution mentioned above, it can be said that the EF bond breaking has started at this point. This strain is that with the

TABLE II. Projections of the bonds (Å) in the $[2\bar{2}1]$ direction at the strain 0%.

Bond	EF	ER	EH	ES	ET	FG	FP	FQ	FR
Projection	2.596	1.771	2.584	0.511	1.927	2.598	1.876	0.592	0.825

maximum tensile stress. Thus it can be said that the EF bond (and E′F′ bond) dominates the tensile strength, and that the breaking of this bond mainly means the failure of this boundary. At the strain 21%, the stretching of the EF bond is 15.6% against the perfect Al. This critical stretching is rather shorter than that observed in the SiC boundary,[20,21] where the Si-C bond breaking starts if local bond stretching approaches to about 20%. Of course, in the present case, the interfacial atoms are less-coordinated in contrast to the bulklike four-coordinated configurations of the SiC boundary. And it seems that usual $[1\bar{1}0]$ bonds in Al can sustain larger stretching as the behavior of the EH bond in Fig. 7(a).

After the starting of the EF bond breaking, the increase of the EF bond length and the contraction of the stretched back bonds EH and FG are rather slow in Fig. 7 as compared with the behavior observed in the SiC boundary.[20,21] This feature should be the origin of very slow decrease in the tensile stress after the maximum point in Fig. 4 as discussed above. This feature should be concerned with the difference between covalent bonding and metallic bonding. In *sp*-valent metals, valence electrons with no strong directional or localized characters cause longer ranges of atomic interactions and larger numbers of neighbors as compared with covalent materials, although the present interfacial bonds seem to have different features as will be discussed.

In Fig. 7, the extension rates of back bonds are quite different, which should depend on the projected length of these bonds in the tensile direction. This can be clearly analyzed in Table II. Table II lists the projected bond length in the $[2\bar{2}1]$ direction. The larger the projection of the bond length, the more the bond extends under the strain in this direction. It is clear that the EH and FG bonds has larger projected lengths similar to that of the EF bond. This is the reason why these three bonds have larger extensions.

The projections of these bonds in the $[2\bar{2}1]$ direction are the differences in the x coordinates of the two atoms of the bond. In other words, the projected lengths of the EF, FG, and EH bonds correspond to the interlayer or interface distances between each $\{2\bar{2}1\}$ atomic layers. Thus we perform an additional analysis so as to clarify the changes of the position of each $\{2\bar{2}1\}$ atomic layer, namely, the x coordinate of each atom, in the tensile test. To analyze this, we calculated the moving distance of atoms constituting the bonds in Fig. 7 as a function of tensile strain, as shown in Fig. 8. The moving distance in the $[2\bar{2}1]$ direction is defined by

$$x_\varepsilon - (1+\varepsilon)x_0, \tag{5}$$

where x_ε and x_0 are the x coordinates of atoms at the strain ε and 0, respectively. Therefore, the moving distance is relative to atomic positions when the cell is linearly extended by strain ε, though this is not the case due to the atomic relaxation. Obviously, an increase of the moving distance implies the right move (i.e., the $[2\bar{2}1]$ direction in Fig. 1), while a decrease implies the left move (i.e., the $[\bar{2}\bar{2}1]$ direction), relative to the linear extension of the x coordinates at the strain 0%.

It should be noted that the results of atoms S and R and those of T and Q are symmetrically equivalent, respectively. For small strains until 5%, all the atoms have local displacements deviating from the linear change, which should be related to the relaxation of the initial compressive stress in the supercell. However, after the strain 5%, the moving distance of all atoms is almost the constant value until the strain 19%. This means that the x coordinate of each atom extends linearly after the strain 5% and until 19%. Namely, it can be said that interlayer or interface distances between each $\{2\bar{2}1\}$ atomic layers extend rather uniformly from the strain 5% to the strain 19%. From the strain over 19%, all the atoms move differently, and the relative distances between the x coordinates of atoms deviate from the linear change. Atoms E and F move to contrary directions from the strain 21%, which means the rapid increase of the interfacial distance, consistent with the rapid increase of the EF bond

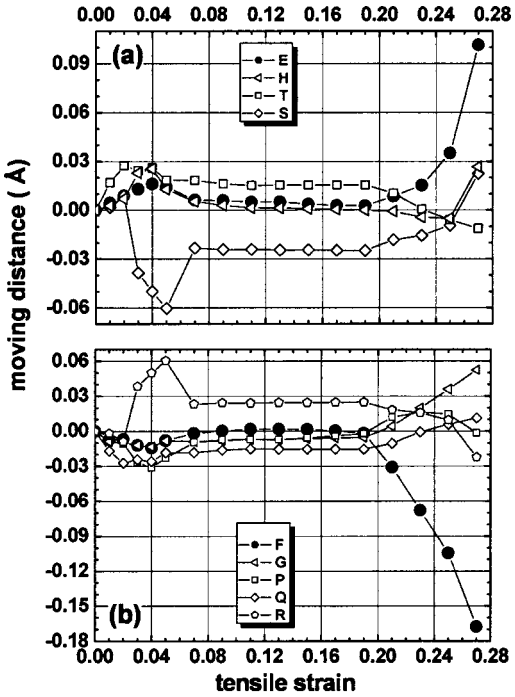

FIG. 8. Moving distance of the atoms as a function of tensile strain. The moving distance of atom E and its nearest neighbors H, S, and T is shown in (a) and of atom F and its nearest neighbors G, P, Q, R is shown in (b).

length in Fig. 7. Other atoms move so as to reduce the projected length of the bonds with atom E or F relatively to the linear extension.

The most striking result is that the extension of the interfacial EF bond increases almost linearly from the strain 5% to the strain 19%, and its linear coefficient is almost the same as those of the FG and EH bonds in the bulk region, as shown in Fig. 7. Similarly, we can see in Fig. 8 that the interlayer distances between the $\{2\bar{2}1\}$ atomic layers of atoms G, F, E, and H extend uniformly from the strain 5% to the strain 19%. This means that the interface distance between the layers of E and F extends similarly to the bulk interlayers between the layers of G and F and those of E and H. This is very strange because of the reduced number of interfacial bonds and the different directions of reconstructed bonds across the interface. Therefore we have to consider the special strength of the reconstructed EF bond at the interface. In the stable configuration without strain, the EF bond is shorter than the bulk bond, and has increased bond charge with similar features to covalent bonds. The formation of the present strong interfacial bonds should be the same kind of phenomena as recently observed in *ab initio* calculations of Al vacancies,[30,31] Al surfaces,[32] and shear distortion of Al.[33] It can be said that strong local bonds with some covalent characters are formed for less-coordinated or greatly distorted atoms in Al, quite differently from most of other simple or noble metals. In the tensile test, such kind of strong bonds can sustain the tensile stress, which results in the extension of the interface at almost the same rate as the bulk interlayer until the start of the failure, though the number of interfacial bonds decreases. The reason that the failure starts at the interface should be the reduced number of bonds across the interface and the presence of the low-density regions, and thus the local stress is concentrated on the reconstructed bonds for larger strains.

Finally it should be mentioned that there is another interfacial bond, i.e., ER bond. Its bond length in the stable configuration is 2.874 Å, 2.9% longer than that of perfect Al, which indicates that it should be a weak bond. The bond length variation with the strain [Fig. 7(a)] shows that it extends linearly until the strain 23%. This implies the ER bond is broken after the breaking of the EF bond. Linear coefficient of the ER bond is similar to that of FP bond until 19%, because the projected length of ER bond in the tensile direction is similar to that of FP bond (see Table II). Both the linear coefficient and the projected length are smaller than those of EF bond. Hence EF bond dominates the tensile strength of the present boundary.

IV. CONCLUSIONS

The *ab initio* tensile test has been applied to an Al grain boundary by using the *ab initio* pseudopotential method. The theoretical tensile strength is 9.50 GPa for the Al $\Sigma 9$ grain boundary at the strain 21%. The failure starts from the interface. As compared with the theoretical tensile strength in the direction [001] or [111] of Al single crystal, the present boundary is still strong due to the boundary reconstruction. The reconstructed bonds have shorter bond length and increased bond charge in the stable configuration. We found that the interface extends at almost the same rate as the bulk interlayer before the failure starts in spite of the reduced number of interfacial bonds, which indicates that the reconstructed interfacial bonds are really strong mechanically. This feature can be regarded as a typical property of Al that strong local bonds are formed for less-coordinated atoms at defects.

ACKNOWLEDGMENTS

The research is supported by National Natural Science Foundation of China (NSFC). Grant No. 50201002. M.K. thanks Professor S. Ogata for fruitful discussion.

*Present address: Department of Materials Science and Engineering, University of Utah, Salt Lake City, UT 84102. Electronic address: LGH@eng.utah.edu

[1] J.W. Morris, Jr. and C.R. Krenn, Philos. Mag. A **80**, 2827 (2002).
[2] G.P. Hohenberg and W. Kohn, Phys. Rev. **136**, B864 (1964).
[3] W. Kohn and L.J. Sham, Phys. Rev. **140**, A1133 (1965).
[4] P. Ŝandera, J. Pokluda, L.G. Wang, and M. Ŝob, Mater. Sci. Eng., A **234–236**, 370 (1997).
[5] M. Ŝob, L.G. Wang, and V. Vitek, Mater. Sci. Eng., A **234–236**, 1075 (1997).
[6] M. Ŝob, L.G. Wang, and V. Vitek, Philos. Mag. B **78**, 653 (1998).
[7] D. Roundy, C.R. Krenn, M.L. Cohen, and J.W. Morris, Jr., Phys. Rev. Lett. **82**, 2713 (1999).
[8] W. Li and T. Wang, J. Phys.: Condens. Matter **10**, 9889 (1998).
[9] V.B. Deyirmenjian, V. Heine, M.C. Payne, V. Milman, R.M. Lynden-Bell, and M.W. Finnis, Phys. Rev. B **52**, 15191 (1995).
[10] W. Li and T. Wang, Phys. Rev. B **59**, 3993 (1999).
[11] S. Ogata, N. Hirosaki, C. Kocer, and H. Kitagawa, Phys. Rev. B **64**, 172102 (2001).
[12] D. Roundy, C.R. Krenn, M.L. Cohen, and J.W. Morris, Jr., Philos. Mag. A **81**, 1725 (2001).
[13] D. Roundy and M.L. Cohen, Phys. Rev. B **64**, 212103 (2001).
[14] W. Luo, D. Roundy, M.L. Cohen, and J.W. Morris, Jr., Phys. Rev. B **66**, 094110 (2002).
[15] F.J. Ribeiro, D. Roundy, and M.L. Cohen, Phys. Rev. B **65**, 153401 (2002).
[16] C.R. Krenn, D. Roundy, M.L. Cohen, D.C. Chrzan, and J.W. Morris, Jr., Phys. Rev. B **65**, 134111 (2002).
[17] R. Car and M. Parrinello, Phys. Rev. Lett. **55**, 2471 (1985).
[18] M.P. Teter, M.C. Payne, and D.C. Allan, Phys. Rev. B **40**, 12 255 (1989).
[19] M.C. Payne, M.P. Teter, D.C. Allan, T.A. Arias, and J.S. Joannopoulos, Rev. Mod. Phys. **64**, 1045 (1992).
[20] M. Kohyama, Philos. Mag. Lett. **79**, 659 (1999).
[21] M. Kohyama, Phys. Rev. B **65**, 184107 (2002).
[22] C. Molteni, G.P. Francis, M.C. Payne, and V. Heine, Phys. Rev. Lett. **76**, 1284 (1996).
[23] C. Molteni, N. Marzari, M.C. Payne, and V. Heine, Phys. Rev. Lett. **79**, 869 (1997).
[24] G.-H. Lu, A. Suzuki, A. Ito, M. Kohyama, and R. Yamamoto, Modell. Simul. Mater. Sci. Eng. **8**, 727 (2000).

[25] G.-H. Lu, A. Suzuki, A. Ito, M. Kohyama, and R. Yamamoto, Philos. Mag. Lett. **81**, 757 (2001).
[26] G.-H. Lu, M. Kohyama, and R. Yamamoto, Mater. Trans., JIM **42**, 2238 (2001).
[27] G.-H. Lu, T. Tamura, M. Kohyama, and R. Yamamoto, J. Iron Steel Technology Special Issue, 456 (2002).
[28] G.-H. Lu, M. Kohyama, and R. Yamamoto, Philos. Mag. Lett. **83**, 159 (2003).
[29] G.-H. Lu, A. Suzuki, A. Ito, M. Kohyama, and R. Yamamoto, Mater. Trans., JIM **44**, 337 (2003).
[30] K. Carling, G. Wahnström, T.R. Mattsson, A.E. Mattsson, N. Sandberg, and G. Grimvall, Phys. Rev. Lett. **85**, 3862 (2000).
[31] T. Uesugi, M. Kohyama, and K. Higashi, Phys. Rev. B **68**, 184103 (2003).
[32] P.J. Feibelman, Phys. Rev. Lett. **65**, 729 (1990).
[33] S. Ogata, J. Li, and S. Yip, Science **298**, 807 (2002).
[34] M.J. Mills and M.S. Daw, in *High Resolution Electron Microscopy of Defects in Materials*, edited by R. Sinclair, D.J. Smith, and U. Duhmen, MRS Symposia Proceedings No. 183 (Materials Research Society, Warrendale, 1990), p. 15.
[35] See, for example, W.E. Pickett, Comput. Phys. Rep. **9**, 115 (1989).
[36] D.M. Ceperley and B.J. Alder, Phys. Rev. Lett. **45**, 566 (1980).
[37] J. P. Perdew and A. Zunger, Phys. Rev. B **23**, 5048 (1981).
[38] D.M. Bylander, L. Kleinman, and S. Lee, Phys. Rev. B **42**, 1394 (1990).
[39] G.P. Kerker, Phys. Rev. B **23**, 3082 (1981).
[40] M. Kohyama, Modell. Simul. Mater. Sci. Eng. **4**, 397 (1996).
[41] H.J. Monkhorst and J.D. Pack, Phys. Rev. B **13**, 5188 (1976).
[42] N. Troullier and J. L. Martins, Phys. Rev. B **43**, 1993 (1991).
[43] J. Hoekstra and M. Kohyama, Phys. Rev. B **57**, 2334 (1998).
[44] L. Kleinman and S.M. Bylander, Phys. Rev. Lett. **48**, 1425 (1982).
[45] P. K. Lam and M. L. Cohen, Phys. Rev. B **24**, 4224 (1981).
[46] Nielsen and R.M. Martin, Phys. Rev. B **32**, 3780 (1985); **35**, 9308 (1987).
[47] S. Ogata (private communication).
[48] N. Gane, Proc. R. Soc. London, Ser. A **317**, 367 (1970).
[49] E.A. Brandes, *Smithells Metals Reference Book*, 6th ed. (Butterworths Heinemann, London, 1983).
[50] C. Kittel, *Introduction to Solid Physics*, 7th ed. (Wiley, New York, 1996).